Comput. Methods Appl. Mech. Engrg. 198 (2009) 2360–2367

Contents lists available at ScienceDirect

Comput. Methods Appl. Mech. Engrg.

journal homepage: www.elsevier.com/locate/cma

High performance simulations of electrokinetic flow and transport in microfluidic chips

Pablo A. Kler, Ezequiel J. López, Lisandro D. Dalcín *, Fabio A. Guarnieri, Mario A. Storti

Centro Internacional de Métodos Computacionales en Ingeniería (CIMEC), Instituto de Desarrollo Tecnológico para la Industria Química (INTEC), Consejo Nacional de Investigaciones Científicas y Tecnológicas (CONICET), Universidad Nacional del Litoral (UNL), (S3000GLN) Santa Fe, Argentina

ARTICLE INFO

Article history:
Received 23 October 2008
Received in revised form 10 February 2009
Accepted 18 February 2009
Available online 26 February 2009

Keywords:
Microfluidics chips
Electrokinetic flow
Mass transport
Parallel computing
Additive Schwarz methods

ABSTRACT

This article discusses high performance numerical simulations of electrokinetic flow and transport phenomena in microfluidic chips. Modeling grounds on conservation equations of mass, momentum and electric charge in the framework of continuum mechanics. Two examples of interest in microfluidics are considered as study cases. Three dimension effects and whole chip geometries are taking into account. All numerical simulations presented are performed with *PETSc-FEM* within a Python programming environment employing parallel computing. Computation time and parallel efficiency are measured in order to study additive Schwarz method performance as domain decomposition technique in solving common ill-conditioned microfluidics problems.

1. Background

Micro-total analysis systems (μ-TAS) perform the functions of large analytical devices in small units [1]. They are used in a variety of chemical, biological and medical applications. The benefits of μ-TAS are a reduction of consumption of samples and reagents, shorter analysis times, greater sensitivity, portability and disposability. There has been a huge interest in these devices in the past decade that led to a commercial range of products.

Most microfluidic systems have been successfully fabricated in glass or silica [2]. Microscopic channels are defined in these substrates using *photolithography* and *micromachining*, whose materials and fabrication methods were adopted from the microelectronics industry. However, for the purposes of rapid prototyping and testing of new concepts, the fabrication processes are slow and expensive.

Numerical simulations of on-chip processes can serve to reduce the time from concept to chip [3]. The most interesting aspect of computational simulation of microfluidic chips is the multiphysics nature which combines fluidics, transport, thermal, mechanics, electronics and optics with chemical, biological thermodynamics and reaction kinetics. Additionally, studying theses effects is a challenging problem from the numerical point of view. They comprise geometrical scales that span six orders of magnitude: from the millimetric size of reservoirs, through the micrometric width of channels, to the nanometric thickness of the electric double layer at interfaces.

Some of the first numerical simulations of fluid flow and species transport for microfluidic chips were addressed to electrokinetic focusing and sample dispensing techniques [4–6], and they employed an algorithm based on finite volume method in a structured grid. Bianchi et al. [7] performed 2D finite element simulations artificially increasing the EDL thickness. Chatterjee [8] developed a 3D finite volume model to study several applications in microfluidics. More recently, Kler et al. [9] developed a 3D FEM model to describe the transport of non-charged species by electroosmotic flow (EOF), and Barz and Ehrhard [10] developed a fully-coupled modeling for electrokinetic flow in microfluidic devices employing 2D finite elements.

Parallel computations and domain decomposition techniques in electrokinetic flow and transport have not been extensively explored. Tsai et al. [11] presented a 2D parallel finite volume scheme to solve electroosmotic flow in L-shaped microchannels and Kler et al. [12] presented 3D FEM simulations for electrokinetic flow in complex microgeometries. Simulations of electrophoretic processes employing this techniques were performed by Chau et al. [13,14] using finite difference method and Kler et al. [15] using FEM, both in 3D.

In this paper a high performance 3D finite element model for the simulation of electrokinetic flow and transport in microfluidic chips is presented. Parallel computing and classical domain

* Corresponding author. Tel./fax: +54 (0) 342 4511594.
E-mail addresses: pkler@intec.unl.edu.ar (P.A. Kler), ejlopez@santafe-conicet.gob.ar (E.J. López), dalcinl@intec.unl.edu.ar (L.D. Dalcín), aguarni@santafe-conicet.gob.ar (F.A. Guarnieri), mstorti@intec.unl.edu.ar (M.A. Storti).

0045-7825/$ - see front matter © 2009 Elsevier B.V. All rights reserved.
doi:10.1016/j.cma.2009.02.028

decomposition techniques are employed in order to solve the problems. Wall-clock time and parallel efficiency are measured in order to study additive Schwarz method performance as domain decomposition technique in solving ill-conditioned problems in microfluidics applications.

2. Theoretical modeling

In this section a mathematical model to simulate 3D and time-dependent electrokinetic flow and transport phenomena in microchannels is presented. First the fluid mechanics and the basis of electroosmotic flow is discussed, then the species transport equation is presented. We considered the case of microchannel networks filled with an aqueous strong electrolyte solution.

2.1. Governing equations

Electrokinetic effects arise when the mobile portion of the diffuse double layer (see Section 2.2.1) and an electric field interact in the viscous shear layer [16]. Depending on the nature of this electric field, different electrokinetic phenomena will appear. When there exists a movement of the liquid caused by the migration of ions under the effects of an external electric field, in relation to some charged solid wall, we are in presence of electroosmotic flow. In the framework of continuum fluid mechanics, fluid velocity $\mathbf{u}$, pressure p, and electric $\mathbf{E}$ fields are governed by the following set of coupled equations [17–19]:

$$\nabla \cdot \mathbf{u} = 0, \tag{1}$$

$$\rho\left(\frac{\partial \mathbf{u}}{\partial t} + \mathbf{u} \cdot \nabla \mathbf{u}\right) = \nabla \cdot \boldsymbol{\sigma} + \rho_e \mathbf{E}, \tag{2}$$

$$\nabla \cdot (\epsilon \mathbf{E}) = \rho_e. \tag{3}$$

Eq. (1) expresses the conservation of mass for incompressible fluids. Eq. (2) (Navier–Stokes equation) expresses the conservation of momentum for Newtonian fluids of density ρ, viscosity μ, and stress tensor $\boldsymbol{\sigma} = -p\mathbf{I} + \mu(\nabla \mathbf{u} + \nabla \mathbf{u}^T)$, subjected to electric field $\mathbf{E}$. The last term on the right hand side of Eq. (2) represents the contribution of electrical forces to the momentum balance, where $\rho_e = F \sum z_j c_j$ is the electric charge density of the electrolyte solution, obtained as the summation over all type-j ions, with valence z_j and molar concentration c_j, and F is the Faraday constant.

Eq. (3) (Poisson equation) establishes the relation between electric field and charge distributions in the fluid of permittivity ϵ that, in the present work, is considered constant due to its usually weak dependency on ion's concentration [10]. Here it is relevant to mention that the ion distributions c_k (to be included in Eqs. (2) and (3)) through ρ_e must be derived from Nernst–Planck equation, which accounts for the flux of type-j ions due to electrical forces, fluid convection and Brownian diffusion [16].

The transport of sample species and buffer electrolyte constituents can be modeled by a linear superposition of migrative, convective and diffusive transport mechanisms and a reactive term. Considering only strong electrolytes, reactive term vanishes. Thus in a non-stationary mode, for the j-type specie, the present work considers the following transport equation:

$$\frac{\partial c_j}{\partial t} + \mathbf{u} \cdot \nabla c_j = D_j \nabla^2 c_j - \nabla \cdot (v_j z_j c_j F \mathbf{E}), \tag{4}$$

which governs the molar concentration c_j of species in the electrolyte solution. In Eq. (4), D_j is the diffusion coefficient, v_j is the mobility, and F is the Faraday constant. The resulting system (Eqs. (1)–(4)) is strongly coupled, but with certain assumptions, this coupling can be avoided (see Section 2.2).

2.2. Electrokinetic phenomena

Generally, most substrates will acquire a surface electric charge when brought into contact with an aqueous medium. Some of the charging mechanisms include ionization, ion adsorption, and ion dissolution. The effect of any charged surface in an electrolyte solution will be to influence the distribution of nearby ions in the solution. Ions of opposite charge to that of the surface (*counterions*) are attracted towards the surface while ions of like charge (*coions*) are repelled from the surface. This attraction and repulsion, when combined with the mixing tendency resulting from the random thermal motions of the ions, leads to the formation of an *electric double layer*.

The electric double layer is a region close to the charged surface in which there is an excess of counterions over coions to neutralize the surface charge, and these ions are spatially distributed in a "diffuse" manner. Evidently there is no charge neutrality within the double layer because the number of counterions will be large compared with the number of coions.When moving away from the surface, the potential progressively decreases, and then vanishes in the liquid phase.

2.2.1. Electric double layer theory

Consider a simple fully dissociated symmetrical salt in solution for which the number of positive and negative ions are equal, so

$$z_+ = -z_- = z. \tag{5}$$

When this electrolyte solution is brought into contact with a solid such that the surface of contact becomes electrically charged, at the stationary state, the concentrations of positive and negative ions can be modeled with the following Boltzmann distribution [20,21]

$$c_\pm = c_0 \exp\left(\frac{\mp zF}{RT}\phi\right); \tag{6}$$

where ϕ is the electric potential, c_0 is the bulk salt concentration, R is the ideal gas constant and T is the absolute temperature and the $\pm$ signs are in a such way that Eq. (6) models the situation of a positively charged wall. In the case of a negatively charged wall, the $\pm$ sign inverts at the right hand side of Eq. (6). Clearly, the ion concentrations far from the surface $c_\pm \to c_0$ as $\phi \to 0$.

Under the above assumptions, the electric charge density is

$$\begin{aligned}\rho_e &= F\sum_k z_k c_k = F\left[+zc_0 \exp\left(\frac{-zF}{RT}\phi\right) - zc_0 \exp\left(\frac{+zF}{RT}\phi\right)\right] \\ &= 2zc_0 F \sinh\left(-\frac{zF}{RT}\phi\right);\end{aligned} \tag{7}$$

and the electric field $\mathbf{E}$ is related to the electric potential ϕ through

$$\mathbf{E} = -\nabla\phi. \tag{8}$$

Eqs. (7) and (8) can be inserted in the Poisson equation (3) to finally obtain

$$-\nabla^2\phi = \frac{2zc_0F}{\epsilon}\sinh\left(-\frac{zF}{RT}\phi\right). \tag{9}$$

The electric potential ϕ obtained through solving the Poisson–Boltzmann equation (9) can then be employed for determining the electric field $\mathbf{E}$ (Eq. (8)) and the electric charge density ρ_e (Eq. (7)). The electrical forces can then be computed and entered in the momentum equation (2).

2.2.2. Electric double layer thickness

The electric double layer thickness may be approximately quantified through the *Debye length* [10,22],

$$\lambda_D = \sqrt{\frac{\epsilon RT}{2Ic_0F^2}}; \tag{10}$$

where I is the dimensionless ionic strength calculated as

$$I = \frac{1}{2}\sum_j z_j^2 \frac{c_{j,bulk}}{c_0}. \tag{11}$$

The *Debye length* represents the position where the electrical potential energy is approximately equal to the thermal energy of the counterions. It is obtained by neglecting the presence of coions and solving a simplified Poisson problem, employing a linearization known as *Debye–Hückel* approximation, which is valid for electrokinetic potentials less than $2RT/F$ [23].

For the ionic concentrations normally used in practice, λ_D is on the order of 10 nm. Away from the interface, at distances beyond λ_D, the bulk of the fluid is electrically neutral.

2.2.3. Electroosmotic flow and slip velocity approximation

Electroosmotic flow in microchannels grounds on the existence excess of ions in the fluid near solid walls. When an external electric field is applied in the axial direction of a channel, the electrical forces acting on excess ions drag the surrounding liquid and then electroosmotic flow develops.

For thin electric double layer in relation to the channel width, electroosmotic phenomena is confined to regions close to channel walls. Under these conditions, the electroosmotically driven flow can be regarded as the result of an electrically-induced *slip velocity*; its magnitude can be approximated by [16,22]

$$\mathbf{u}_{EO} = -\frac{\epsilon\zeta}{\mu}\mathbf{E}; \tag{12}$$

where ζ is the electrokinetic potential.

Further, $\mathbf{u}_{EO}$ can be used as a boundary value at the channel walls. This possibility greatly simplifies calculations since ion distributions are decoupled from Navier–Stokes and Poisson equations. In fact, if ion concentrations are assumed to be uniform for the buffer components (except in the close vicinity of the charged interface), and sufficiently low, for the sample components, in order to not affect the charge density nor the permittivity, the right hand side of Eq. (3) vanishes, as well as the last term of Eq. (2). This assumptions enable us to solve independently Eqs. (1)–(4).

Moreover the restriction mentioned above, the slip velocity approximation is valid when the *Debye–Hückel* approximation is valid [24], and for small values of λ_D/h (where h is the channel width), which is usually the case in micro-scale channels at moderate ionic concentrations ($\approx 10^{-3}$ M). Nevertheless, at very low ionic concentrations ($\approx 10^{-6}$ M), or in case of nanoscale channels, λ_D/h approaches one, indicating that the electric double layer from opposing surfaces overlap. In that case, approximation (12) does not apply and the full problem must be solved.

Other aspects of this approximation deserve consideration, like wall rugosity and the influence of the applied potential in the EDL distribution, for more details about the physics of the problem and the validity of different assumptions, see [25].

2.3. Classical domain decomposition methods

Domain decomposition methods (DDM) [26] are *divide and conquer* techniques for solving boundary value problem by splitting it into smaller boundary value problems on subdomains and iterating to coordinate the solution between them. The problems on the subdomains are independent, which makes domain decomposition methods suitable for parallel computing on distributed memory architectures. Domain decomposition methods are typically used as preconditioners for Krylov space iterative methods, such as the conjugate gradients (CG) method or generalized minimal residual (GMRES) method.

In non-overlapping methods (also called iterative substructuring methods), the subdomains overlap only on their interface. In primal methods, such as *balancing domain decomposition* (BDD) and the enhanced version BDDC [27], the continuity of the solution across subdomain interfaces is enforced by representing the value of the solution on all neighboring subdomains by the same unknown. In dual methods, such as *finite elements tearing and interconnecting* (FETI), the continuity of the solution across the subdomain interface is enforced by Lagrange multipliers. An enhanced, simplified and better performing version of FETI, known as FETI-DP [28], is hybrid between a dual and a primal method; its performance is essentially the same as the BDDC method. BDD and FETI methods were primarily developed for solving of elliptic boundary value problems.

In overlapping domain decomposition methods, the subdomains overlap by more than the interface. Overlapping domain decomposition methods include the classical Schwarz alternating procedure and the *additive Schwarz method* (ASM) [29]. Schwarz methods can be easily applied to a variety of problems [30,31] and can be implemented in a fully-algebraic manner (i.e. without knowledge of the underlying discrete grids).

2.3.1. Additive Schwarz preconditioning

The original alternating procedure described by Schwarz [32] in 1870 is an iterative method to find the solution of a partial differential equations on a domain which is the union of two overlapping subdomains, by solving the equation on each of the two subdomains in turn, taking always the latest values of the approximate solution as the boundary conditions.

The procedure described above is called the *multiplicative* Schwarz procedure. In matrix terms, this is very reminiscent of a block Gauß–Seidel iteration. The multiplicative Schwarz procedure is not fully parallel at the highest level: some processors have to wait others in order to perform the local work. The analogue of the block Jacobi procedure is known as the *additive* Schwarz procedure. The additive procedure is fully parallel; however, the convergence rate is usually lower.

The application of the additive Schwarz procedure as a preconditioning method for the solution of systems of linear equations can be summarized as follows:

- The support mesh/grid is decomposed into N_s (possibly *overlapping*) subdomains $\Omega_i, i = 1, \ldots, N_s$.
- Each subdomain Ω_i is associated to a local space V_i with the help of a restriction operator R_i. The restriction operator R_i extract from the global vector the unknowns associated with Ω_i, while the extension operators R_i^{T} extends by zeros unknowns from Ω_i to the global vector. The preconditioner operator can then be easily written in matrix terms as

$$P^{-1} = \sum_{i=1}^{N_s} R_i^{\mathrm{T}} A_i^{-1} R_i; \tag{13}$$

  where $A_i = R_i^{\mathrm{T}} A R_i$ are the local matrices associated with the subdomains Ω_i; they are related to the global matrix A through the restriction operators R_i. In the special case of zero overlap, the matrices A_i have entries from contributions originated in the subdomain Ω_i; if the overlap is greater than zero, the matrices A_i have additional entries contributed by neighboring subdomains.
- Any Krylov-based iterative method can then be employed for solving the (left) preconditioned linear system $P^{-1}Ax = P^{-1}b$.

Many factors impact the performance of additive Schwarz preconditioning in the context of parallel iterative methods for the

solution of systems of linear equations. The main ones are summarized in the following list:

- Additive Schwarz methods are normally implemented in such a way that the number of subdomains N_s and the restriction operators R_i are inherited from the previous partitioning of the underlying discrete grid or mesh. The local problems (involving matrix A_i in Eq. (13)) are usually solved by variants of incomplete factorization methods (e.g. ILU(0)). For well-conditioned problems, incomplete factorization methods are the faster alternative regarding to overall wall-clock computing time.
- Iterative methods frequently stagnate when then global problem is ill-conditioned and the local problems are treated with incomplete factorizations. In such cases, the local problems have to be solved either with and inner iterative method or a full direct method (i.e. LU factorization). In either case, as the size of the local subdomain increases, also do the time required for obtaining the local solution. This is specially true when the local solver is based on a LU factorization. In order to employ a direct method and maintaining the size of local problems manageable, local subdomains can be further partitioned at each processor in sub-subdomains. This strategy degrades convergence, but can improve the overall solution time.
- As the overlap increases, convergence rate improves; but computing, communication and memory requirements increase. Ghost vector values have to be gathered from and scattered to neighboring processors at each iteration; matrix values have to be gathered from neighboring processors in a setup phase, and the local problems to solve are larger (in the setup-phase factorization as well as in the backward/forward solves at each iteration). Then, as overlap increases, actual improvements in the total wall-clock time for obtaining the final solution will depend upon the balance between better convergence rates versus the extra costs.
- Finally, for global problems of medium to large scale, as the number of processors assigned to its solution increases, the parallel efficiency decreases. Actually, this behavior is shared for any non-embarrassingly parallel algorithm. As a rule of thumb, each processor have to be in charge of 50,000–100,000 unknowns (depending on computing and network hardware) to achieve parallel speedup.

3. Materials and methods

3.1. Hardware

Simulations were carried out using a Beowulf cluster *Aquiles* [33]. Its hardware consists of 82 disk-less single processor computing nodes with Intel Pentium 4 Prescott 3.0 GHz 2 MB cache processors, Intel Desktop Board D915PGN motherboards, Kingston Value RAM 2 GB DDR2 400 MHz memory, and 3Com 2000ct Gigabit LAN network cards, interconnected with a 3Com SuperStack 3 Switch 3870 48-ports Gigabit Ethernet.

3.2. Software

All numerical simulations presented were performed within a Python programming environment built upon *MPI for Python* [34–36], *PETSc for Python* [37], and *PETSc-FEM* [38,39]. PETSc-FEM is a parallel multiphysics code primarily targeted to 2D and 3D finite elements computations on general unstructured grids. PETSc-FEM is based on MPI and PETSc [40–42], it is being developed since 1999 at the *International Center for Numerical Methods in Engineering* (CIMEC), Argentina. PETSc-FEM provides a core library in charge of managing parallel data distribution and assembly of residual vectors and Jacobian matrices, as well as facilities for general tensor algebra computations at the level of problem-specific finite element routines. Additionally, PETSc-FEM provides a suite of specialized application programs built on top of the core library but targeted to a variety of problems (e.g. compressible/incompressible Navier–Stokes and compressible Euler equations, general advective–diffusive systems, weak/strong fluid–structure interaction). In particular fluid flow computations presented in this article are carried out within the Navier–Stokes module available in *PETSc-FEM*. This module provides the required capabilities for simulating mass transport and incompressible fluid flow through a monolithic *SUPG/PSPG* [43,44] stabilized formulation for linear finite elements. Electric computations are carried out with Laplace's and the Poisson–Boltzmann modules.

4. Numerical simulations

This section presents the results of numerical simulation performed on two study cases. The first case is an example of capillary zone electrophoresis (CZE) in a whole (μ-TAS) geometry including electrodes and reservoirs. The second case deals with electroosmotic flow in nanoscale channels. The values of the relevant physical properties and constants employed in both cases are summarized in Table 1.

4.1. Capillary zone electrophoresis

Previous works related to numerical simulation of electroosmotic flow and electrophoresis have restricted the problem domain to the microchannels by supposing appropriate conditions for the electric potential, velocity field, and concentrations at inlet and outlet regions. In this example, results from numerical simulations performed on a whole microfluidic system domain are presented.

The simulation domain is a cross-shaped microchannel network with vertical wire electrodes at reservoirs. The aim of the example is to show the capability of the numerical method for simulate 3D high aspects ratio geometries, simulating a common situation in practical microfluidics. A more complete analysis of the effects of reservoirs in microfluidics networks can be found in [45]. The channel sections are trapezoidal, with shape and dimensions as shown in Fig. 1.

Electrophoretic injection and separation processes are simulated in order to determine potassium and sodium ion concentrations. During the injection stage, potentials at the electrodes are selected in such a way that the intersection region is filled with a precise sample volume to be analyzed. In the separation stage, potentials at the electrodes are appropriately selected in order to

Table 1
Physical constants and properties.

Property/constant	Symbol	Value	Unit
Density	ρ	1000	kg/m^3
Viscosity	μ	10^{-3}	kg/m s
Ionic valence	z	1	–
Electrokinetic potential	ζ	$-4 \cdot 10^{-2}$	V
Temperature	T	300	K
Gas constant	R	8.31	J/mol K
Faraday constant	F	96485	C/mol
Permittivity	ϵ	$80 \times 8.85 \cdot 10^{-12}$	F/m
Sodium diffusivity	D_{Na}	$1.34 \cdot 10^{-9}$	m^2/s
Sodium mobility	ν_{Na}	$5.18 \cdot 10^{-8}$	$m^2/V\,s$
Potassium diffusivity	D_K	$1.96 \cdot 10^{-9}$	m^2/s
Potassium mobility	ν_K	$7.58 \cdot 10^{-8}$	$m^2/V\,s$

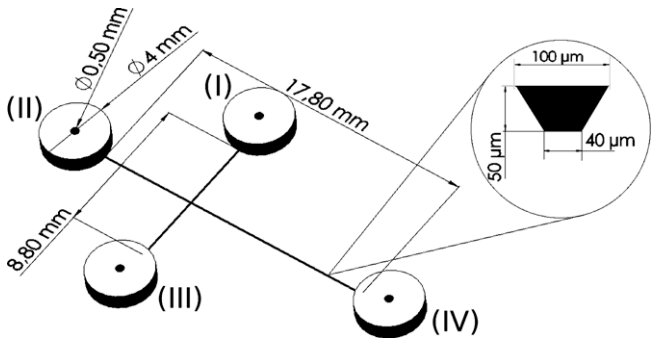

Fig. 1. Geometry of the microchannel network.

achieve different relative velocities for each specie, avoiding leakages at the injection channels.

The complete simulations requires the solution of three subsidiary problems involving charge, mass, momentum and species conservation equations described in Section 1. In order to solve this example some assumptions were made. We have considered strong electrolytes for buffer and sample components, buffer ions concentration is constant in the whole domain, and the sample concentration is adequately low in order to not affect the electric properties of electrolyte solution nor the electric double layer characteristics. Also we have considered that the relation between the channel width and the Debye length ($\lambda = 10$ nm) is large enough to use the Helmholtz–Smoluchowsky slip velocity approximation.

A tetrahedral mesh with 941,056 elements was generated in order to solve the problem, the channel's flow section contains approximately 60 elements. The electric fields are obtained through solving Poisson equation (Eq. (3), with $\rho_e = 0$) for the potential, and employing Dirichlet boundary conditions at electrodes and homogeneous Neumann boundary conditions at channels and reservoirs walls. Applied potentials for different processes are shown in Table 2. The influence of the applied potentials over the EDL distribution is neglected. The validity of this assumption is evaluated measuring the magnitude of the two different electric fields. Then, the electric field applied is approximately 39 kV/m and the EDL associated electric field is in the order of 4000 kV/m, so the assumption is correct. To solve this equation conjugate gradients method was employed as iterative solver, and HYPRE BoomerAMG [46] was chosen as preconditioner.

Table 2
Applied potential for different processes in ECZ.

Process	Potentials (V)			
	Φ_I	Φ_{II}	Φ_{III}	Φ_{IV}
Injection	500.0	250.0	0.0	250.0
Separation	530.0	750.0	530.0	0.0

Fluid velocity was obtained by solving mass conservation equation (1) and Navier–Stokes equation (2) in stationary mode. At the top of the reservoirs, boundary conditions for pressure and velocity were set; for the pressure, Dirichlet boundary conditions with a reference value of zero were imposed, and the velocity direction was constrained to be parallel to the reservoir axis. At the channel walls, the slip velocity approximation (Eq. (12)) was employed as Dirichlet boundary condition. In this example the fact that external pressure gradients were set to zero and zeta potential has a uniform value at channel's surfaces, causes driving force reduces only to its electroosmotic component. Then the velocity profile is merely plane an its average magnitude equal to the slip velocity calculated by Eq. (12), i.e. 1.1 mm/s.

Finally, transport equation (4) was solved for the concentrations of Na^+ and K^+ ions by employing the electric field and fluid velocity previously obtained. This problem is transient; initial concentrations (at $t = 0$ s) were set to zero everywhere except at one of the reservoirs.

In solving Eqs. (2) and (4) for this problem, additive Schwartz method was used as a left preconditioner, with one layer of overlapping between subdomains, with a maximum size of 2000 unknowns in each subdomain. GMRES was employed as iterative solver, and LU factorization was used in each subdomain.

Fig. 2 shows sample distribution in the central region of the cross-network, previous to the separation process, and mesh details in the region near the electrode. Fig. 3 shows concentration distributions of Na^+ and K^+ ions at some moment ($t = 5$ s) during the separation stage.

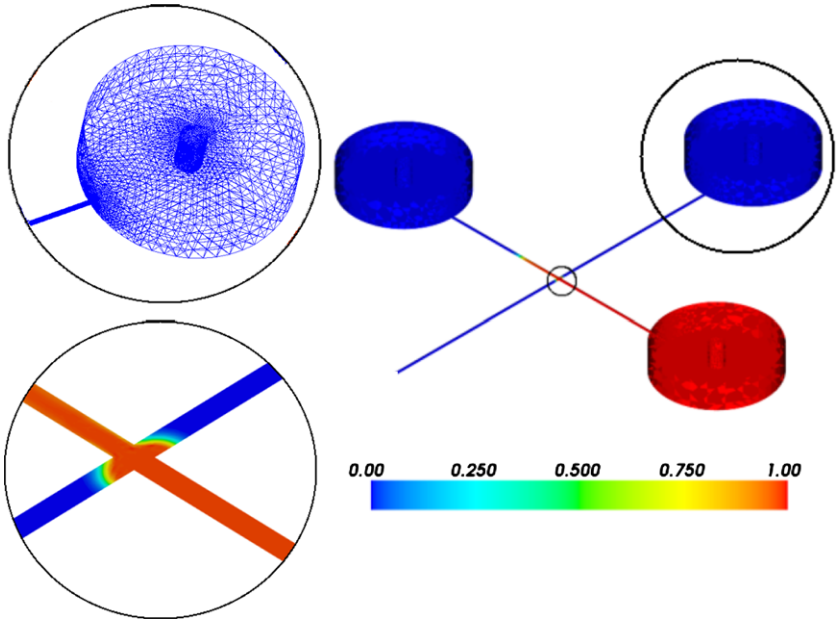

Fig. 2. Sample concentration (mol/m^3) after the injection stage and mesh detail in electrode zone.

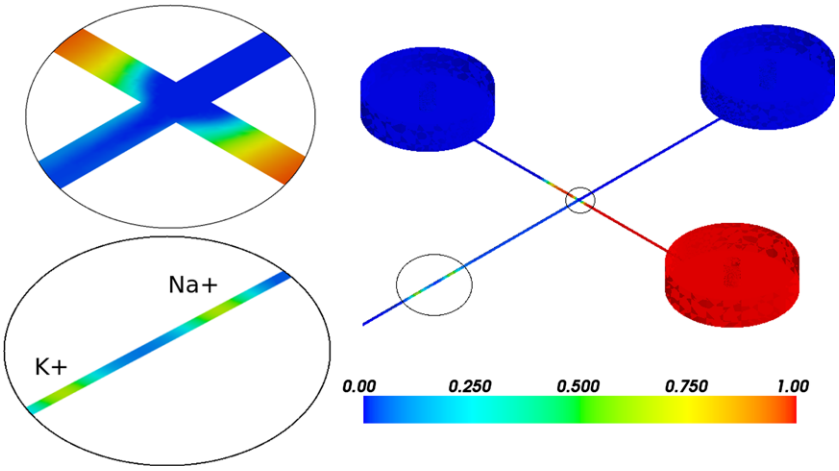

Fig. 3. Na^+ and K^+ ions concentrations (mol/m^3) after separation stage.

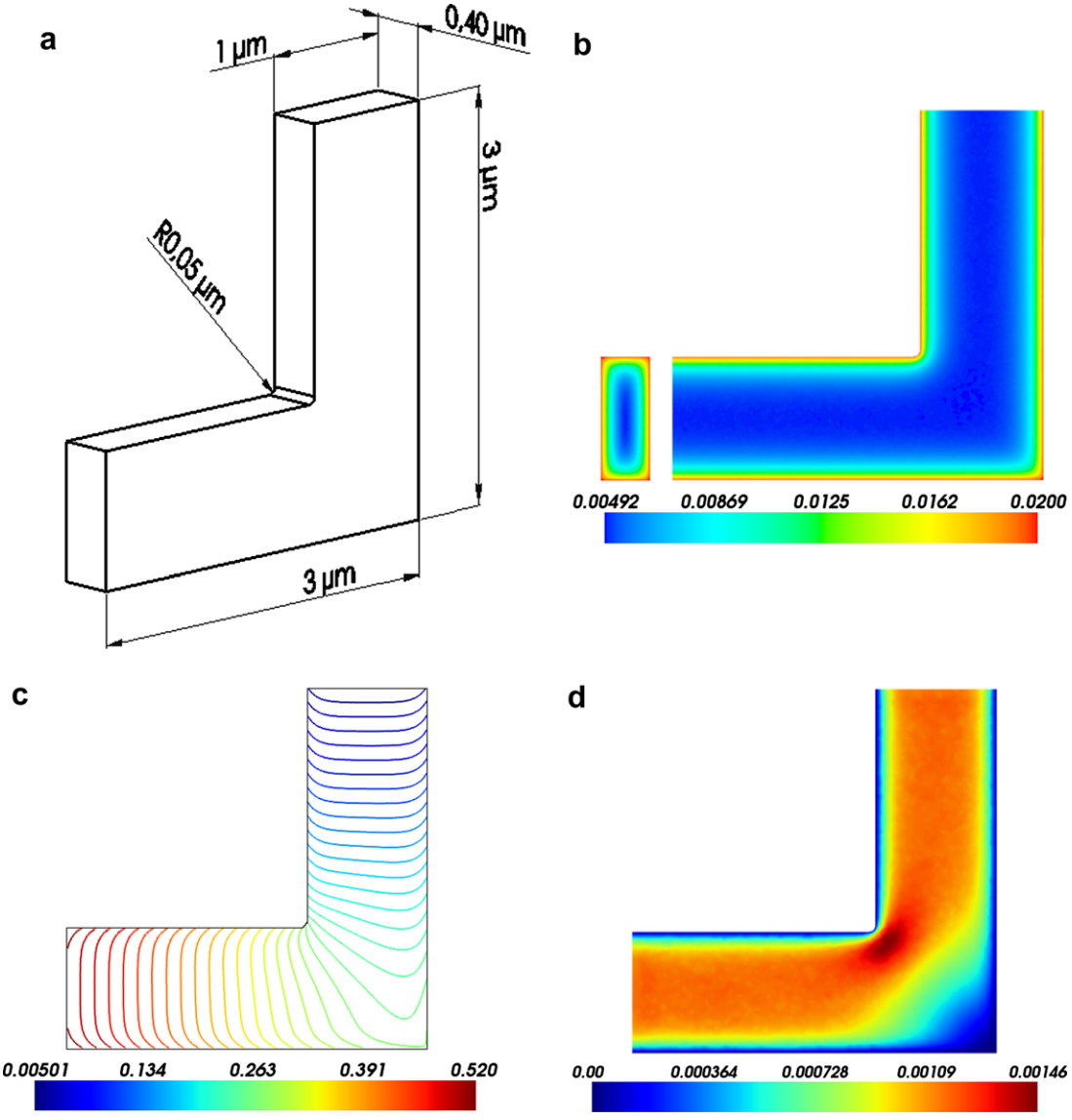

Fig. 4. Model problem for ASM. (a) Geometry; (b) Poisson–Boltzmann potential (V); (c) total potential (V); (d) velocity magnitude (m/s).

4.2. A model problem for additive Schwarz methods

This example explores the applicability of additive Schwarz methods to a model problem of interest in nanoscale fluid dynamics applications. The interest in solving this problem grounds on testing numerical performance of the method, enabling us to measure computation times and parallel efficiency.

Consider an aqueous solution of a simple fully dissociated symmetrical salt which flows on a channel driven by the action of electrical forces originated from external electric fields. The channel has an L-shaped geometry with an horizontal and vertical lengths of 3 μm and a cross-section of 0.4 μm × 1 μm. As the electric double layer thickness (estimated through the Debye length, Eq. (10)) is around 0.1 μm, the slip velocity approximation (Eq. (12)) cannot be employed.

A Laplace potential was computed by solving Eq. (3) with $\rho_e = 0$, Dirichlet boundary conditions of 0.5 V at the inlet and 0 V at the outlet, and homogeneous Neumann boundary conditions at the channel walls. A Poisson–Boltzmann potential was computed by solving the nonlinear equation (9) with Dirichlet boundary conditions of 20 mV (the electrokinetic potential) at the channel walls and homogeneous Neumann boundary conditions at the channel inlet and outlet. The solution for Poisson–Boltzmann potential is shown in Fig. 4b. The Laplace and Poisson–Boltzmann potentials were added-up in order to determine a total potential. Isolines of the total potential are shown in Fig. 4c.

Finally, Navier–Stokes equations are solved by entering the electrical forces as shown in Eq. (2). Electrical forces are determined from the total potential and Poisson–Boltzmann potential through Eqs. (7) and (8). Non-slip velocity boundary conditions are imposed at channel walls, and homogeneous Dirichlet boundary conditions are employed for pressure at the inlet and outlet. The computed velocity magnitude is shown in Fig. 4d.

The L-shaped channel domain was discretized with a tetrahedral mesh with 569,791 nodes, 3,483,613 elements and 20,025,163 degrees of freedom. The rest of this subsection explores the issues commented previously by applying the additive Schwarz preconditioner to the model problem.

Although the problem at hand is essentially linear, it was solved as a full nonlinear one employing two iteration of a standard Newton method. In all the cases, the final (outer, nonlinear) residual norm was reduced by a factor of around 10^{-6}.

The linear systems at each nonlinear step were solved with GMRES(300) (i.e. GMRES restarted at 300 iterations) by defining a fixed relative tolerance of 10^{-4} for the reduction of the initial (inner, linear) residual norm.

The additive Schwarz method was employed as a left preconditioner within GMRES iterations. Being the global linear systems of saddle-point nature, they are ill-conditioned. Incomplete factorizations methods cannot be practically employed for the local problems, as this leads to GMRES stagnation. Thus, the local problems were solved by employing full direct methods and aggressive subdomain sub-partitioning at each processor. The sub-partitioning was performed on the adjacency graph obtained from the local, *diagonal* part of the global sparse matrix with the help of METIS [47] library.

In all test cases, wall-clock time measurements do not account for the time required for evaluating and assembling residual vectors and Jacobian matrices, but only for the time spent in solving the linear systems. Parallel efficiency was computed by taking as reference the timings of the runs performed on the smaller number of processes, i.e. $E_p = (P_{\min} T_{P_{\min}})/(pT_p)$, where $p = \{P_{\min}, \ldots, P_{\max}\}$ is the set of number of processes employed and T_p is the wall-clock time measurement with p processes.

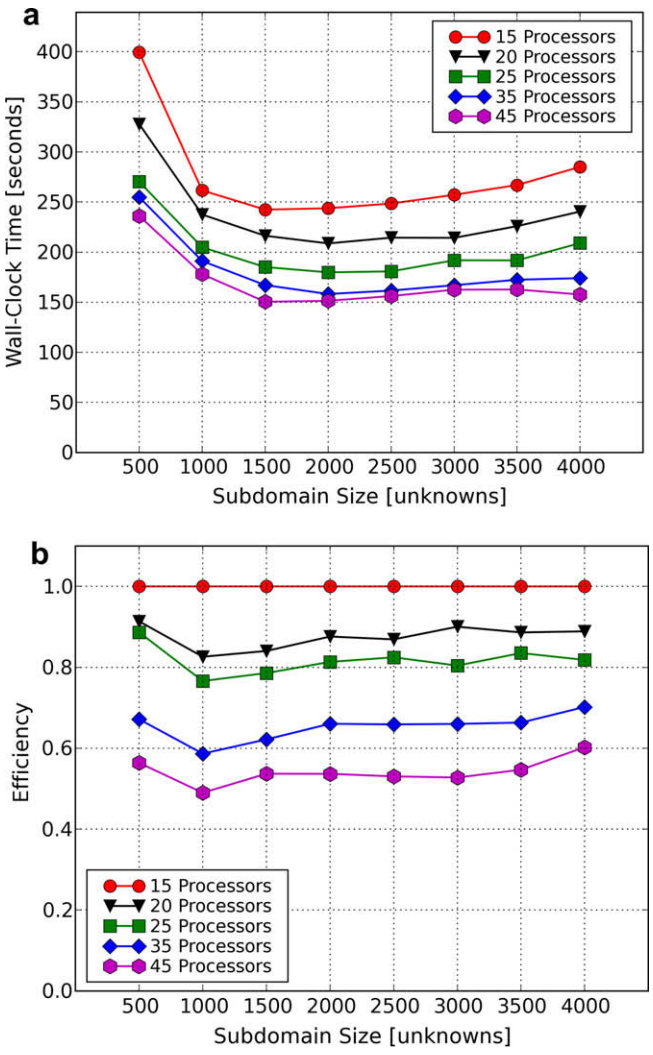

Fig. 5. Additive Schwarz preconditioning.

The problem at hand was solved on 15, 20, 25, 35 and 45 processors. Fig. 5 shows wall-clock time measurements and parallel efficiency for the additive Schwarz preconditioner with overlap zero. The optimal subdomain size seems to be around 1500 unknowns. Clearly, as the number of processors increase beyond some limit, the required wall-clock time for obtaining the solution does not decrease but stagnates.

5. Conclusions

A 3D finite element model for the simulation of electrokinetic flow and transport phenomena in microfluidic chips was presented. Two examples of interest were considered. Electrophoretic separation of ions was modeled and solved in a complete chip geometry. A nanofluidics model problem was solved in order to confirm the applicability and good performance of additive Schwarz preconditioners in these kind of problems. Measured wall-clock time and parallel efficiency are comparable with results reported on related works in the area [13,14].

From a practical point of view, the considered computational approach seems to be a suitable way to solve medium to large scale problems arising in the modeling and design μ-TAS and others applications involving electrokinetic flow and transport phenomena in microfluidics.

Acknowledgements

This work has received financial support from *Consejo Nacional de Investigaciones Científicas y Técnicas* (CONICET, Argentina, Grants PIP 02552/00, PIP 5271/05), *Universidad Nacional del Litoral* (UNL, Argentina, Grant CAI+D 2005-10-64), and *Agencia Nacional de Promoción Científica y Tecnológica* (ANPCyT, Argentina, Grants PICT 12-14573/2003, PME 209/2003).

The authors make extensive use of freely available software such as GNU/Linux operating system, GCC compilers, Python, MPICH and OpenMPI implementations, PETSc libraries, ParaView and others. Many thanks to the open source community for those excellent products.

References

[1] D. Reyes, D. Iossifidis, P. Auroux, A. Manz, Micro total analysis systems. 1. Introduction, theory, and technology, Anal. Chem. 74 (12) (2002) 2623–2636.
[2] M. Madou, Fundamentals of Microfabrication: The Science of Miniaturization, second ed., CRC Press, 2002.
[3] D. Erickson, D. Li, Integrated microfluidic devices, Anal. Chim. Acta 507 (1) (2004) 11–26.
[4] N. Patankar, H. Hu, Numerical simulation of electroosmotic flow, Anal. Chem. 70 (9) (1998) 1870–1881.
[5] S. Ermakov, S. Jacobson, J. Ramsey, Computer simulations of electrokinetic transport in microfabricated channel structures, Anal. Chem. 70 (21) (1998) 4494–4504.
[6] S. Ermakov, S. Jacobson, J. Ramsey, Computer simulations of electrokinetic injection techniques in microfluidic devices, Anal. Chem. 72 (15) (2000) 3512–3517.
[7] F. Bianchi, R. Ferrigno, H. Girault, Finite element simulation of an electroosmotic-driven flow division at a *t*-junction of microscale dimensions, Anal. Chem. 72 (9) (2000) 1987–1993.
[8] A. Chatterjee, Generalized numerical formulations for multi-physics microfluidics-type applications, J. Micromech. Microengrg. 13 (2003) 758–767.
[9] P. Kler, F. Guarnieri, C. Berli, Numerical simulation of electrokinetic flow in microfluidic chips, Mec. Comput. 25 (28) (2006) 2573–2584.
[10] D. Barz, P. Ehrhard, Fully-coupled model for electrokinetic flow and transport in microchannels, PAMM 5 (1) (2005) 535–536.
[11] W.-B. Tsai1, C.-J. Hsieh, C.-C. Chieng, Parallel computation of electroosmotic flow in l-shaped microchannels, in: Sixth World Congress of Structural and Multidisciplinary Optimization, 2005, pp. 4971–4980.
[12] P. Kler, F. Guarnieri, L. Dalcin, Efficient numerical model for electrokinetic flow in microfluidics systems with complex geometries, Mec. Comput. 26 (5) (2007) 485–497.
[13] M. Chau, P. Spiteri, H. Boisson, Parallel numerical simulation for the coupled problem of continuous flow electrophoresis, Int. J. Numer. Methods Fluids 55 (10) (2007) 945–963.
[14] M. Chau, P. Spiteri, R. Guivarich, H. Boisson, Parallel asynchronous iterations for the solution of a 3d continuous flow electrophoresis problem, Comput. Fluids 37 (9) (2008) 1126–1137.
[15] P.A. Kler, F.A. Guarnieri, C.L. Berli, Generalized numerical model for the simulation electrophoretic methods in microfluidic chips, Mec. Comput. 27 (2008) 3367–3380.
[16] R.F. Probstein, Physicochemical Hydrodynamics. An Introduction, second ed., Wiley-Interscience, 2003.
[17] P. Tabeling, Introduction to Microfluidics, Oxford University Press, 2005.
[18] H.A. Stone, A. Stroock, Engineering flows in small devices: microfluidics toward a lab-on-a-chip, Annu. Rev. Fluid Mech. 36 (2004) 381–411.
[19] T. Squires, S. Quake, Microfluidics: fluid physics at the nanoliter scale, Rev. Mod. Phys. 77 (3) (2005).
[20] J.M. Chun Yang, Dongqing Li, Modeling forced liquid convection in rectangular microchannels with electrokinetic effects, Int. J. Heat Mass Transfer 41 (1998) 4229–4249.
[21] R.-J. Yang, L.-M. Fu, Y.-C. Lin, Electroosmotic flow in microchannels, J. Colloids Interface Sci. 239 (2001) 98–105.
[22] R.J. Hunter, Foundations of Colloid Science, second ed., Oxford University Press, 2001.
[23] R.J. Hunter, Zeta Potential in Colloid Science, Academic Press, London, 1981.
[24] J.G. Santiago, Electroosmotic flows in microchannels with finite inertial and pressure forces, Anal. Chem. 73 (10) (2001) 2353–2365.
[25] G. Karniadakis, N. Aluru, A. Beskok, Microflows and Nanoflows: Fundamentals and Simulation, first ed., Springer, 2005.
[26] B.F. Smith, P.E. Bjørstad, W. Gropp, Domain Decomposition: Parallel Multilevel Methods for Elliptic Partial Differential Equations, Cambridge University Press, 1996.
[27] C.R. Dohrmann, A preconditioner for substructuring based on constrained energy minimization, SIAM J. Sci. Comput. 25 (1) (2003) 246–258.
[28] C. Farhat, M. Lesoinne, P. LeTallec, K. Pierson, D. Rixen, FETI-DP: a dual–primal unified FETI method – Part I. A faster alternative to the two-level FETI method, Int. J. Numer. Methods Engrg. 50 (7) (2001) 1523–1544.
[29] A. Frommer, H. Schwandt, A unified representation and theory of algebraic additive Schwarz and multisplitting methods, SIAM J. Matrix Anal. Appl. 18 (4) (1997) 893–912.
[30] M.J. Gander, L. Halpern, Optimized Schwarz waveform relaxation methods for advection reaction diffusion problems, SIAM J. Numer. Anal. 45 (2) (2007) 666–697.
[31] M.J. Gander, L. Halpern, F. Magoulès, An optimized Schwarz method with two-sided robin transmission conditions for the Helmholtz equation, Int. J. Numer. Methods Fluids 55 (2) (2007) 163–175.
[32] H.A. Schwarz, Über einen Grenzübergang durch alternierendes Verfahren, Vierteljahresschr. Naturforsch. Ges. Zur. 15 (1870) 272–286.
[33] M.A. Storti, Aquiles cluster at CIMEC, 2005–2008. <http://www.cimec.org.ar/aquiles>.
[34] L. Dalcín, MPI for Python, 2005–2008. <http://mpi4py.scipy.org>.
[35] L. Dalcín, R. Paz, M. Storti, MPI for Python, J. Parallel Distrib. Comput. 65 (9) (2005) 1108–1115.
[36] L. Dalcín, R. Paz, M.S.J. D'Elia, MPI for Python: performance improvements and MPI-2 extensions, J. Parallel Distrib. Comput. 68 (5) (2008) 655–662.
[37] L. Dalcín, PETSc for Python, 2005–2008. <http://petsc4py.googlecode.com/>.
[38] M.A. Storti, N. Nigro, R. Paz, PETSc-FEM: a general purpose, parallel, multi-physics FEM program, 1999–2008. <http://www.cimec.org.ar/petscfem>.
[39] V.E. Sonzogni, A.M. Yommi, N.M. Nigro, M.A. Storti, A parallel finite element program on a Beowulf cluster, Adv. Engrg. Software 33 (7–10) (2002) 427–443.
[40] S. Balay, K. Buschelman, W.D. Gropp, D. Kaushik, M.G. Knepley, L.C. McInnes, B.F. Smith, H. Zhang, PETSc Web page, 2008. <http://www.mcs.anl.gov/petsc>.
[41] S. Balay, K. Buschelman, V. Eijkhout, W.D. Gropp, D. Kaushik, M.G. Knepley, L.C. McInnes, B.F. Smith, H. Zhang, PETSc users manual, Tech. Rep. ANL-95/11 – Revision 2.3.3, Argonne National Laboratory, 2007.
[42] S. Balay, W.D. Gropp, L.C. McInnes, B.F. Smith, Efficient management of parallelism in object oriented numerical software libraries, in: E. Arge, A.M. Bruaset, H.P. Langtangen (Eds.), Modern Software Tools in Scientific Computing, Birkhäuser Press, 1997, pp. 163–202.
[43] T. Tezduyar, S. Mittal, S. Ray, R. Shih, Incompressible flow computations with stabilized bilinear and linear equal order interpolation velocity pressure elements, Comput. Methods Appl. Mech. Engrg. 95 (1992) 221–242.
[44] T. Tezduyar, Y. Osawa, Finite element stabilization parameters computed from element matrices and vectors, Comput. Methods Appl. Mech. Engrg. 190 (3–4) (2000) 411–430.
[45] C.-C.C. R-J Yang, T-l. Tseng, End effects on electro-osmotic flows in micro-channels, J. Micromech. Microengrg. 15 (2005) 254–262.
[46] R. Falgout, J. Jones, U. Yang, The design and implementation of hypre, a library of parallel high performance preconditioners, Numerical Solution of Partial Differential Equations on Parallel Computers, vol. 51, Springer-Verlag, 2006. pp. 267–294.
[47] G. Karypis, V. Kumar, Multilevel *k*-way partitioning scheme for irregular graphs, J. Parallel Distrib. Comput. 48 (1) (1998) 96–129.